ORIGINAL ARTICLE

Muscarinic and Nicotinic Modulation of Neocortical Layer 6A Synaptic Microcircuits Is Cooperative and Cell-Specific

Danqing Yang[1], Robert Günter[1], Guanxiao Qi[1], Gabriele Radnikow[1] and Dirk Feldmeyer[1,2,3]

[1]Institute of Neuroscience and Medicine (INM-10), Function of Neuronal Microcircuits, Research Centre Jülich, D-52425 Jülich, Germany, [2]Department of Psychiatry, Psychotherapy and Psychosomatics, RWTH Aachen University, D-52074 Aachen, Germany, and [3]Jülich Aachen Research Alliance, Translational Brain Medicine (JARA Brain), D-52074 Aachen, Germany

Address correspondence to Dirk Feldmeyer, Institute of Neuroscience and Medicine (INM-10), Research Centre Jülich, D-52425 Jülich, Germany. Email: d.feldmeyer@fz-juelich.de

Abstract

Acetylcholine (ACh) is known to regulate cortical activity during different behavioral states, for example, wakefulness and attention. Here we show a differential expression of muscarinic ACh receptors (mAChRs) and nicotinic ACh receptors (nAChRs) in different layer 6A (L6A) pyramidal cell (PC) types of somatosensory cortex. At low concentrations, ACh induced a persistent hyperpolarization in corticocortical (CC) but a depolarization in corticothalamic (CT) L6A PCs via M_4 and M_1 mAChRs, respectively. At ~ 1 mM, ACh depolarized exclusively CT PCs via $\alpha_4\beta_2$ subunit-containing nAChRs without affecting CC PCs. Miniature EPSC frequency in CC PCs was decreased by ACh but increased in CT PCs. In synaptic connections with a presynaptic CC PC, glutamate release was suppressed via M_4 mAChR activation but enhanced by nAChRs via $\alpha_4\beta_2$ nAChRs when the presynaptic neuron was a CT PC. Thus, in L6A, the interaction of mAChRs and nAChRs results in an altered excitability and synaptic release, effectively strengthening CT output while weakening CC synaptic signaling.

Key words: acetylcholine, barrel cortex, layer 6, muscarinic receptors, nicotinic receptors

Introduction

Acetylcholine (ACh) has been shown to play a major role in memory processing, arousal, attention, and sensory signaling (Jones 2004; Hasselmo 2006; Herrero et al. 2008; Hasselmo and Sarter 2011; Thiele 2013; Wester and Contreras 2013; Ma et al. 2018). It has been demonstrated that the ACh concentration in the cerebrospinal fluid (CSF) increases during wakefulness and sustained attention from approximately 1 to 1.4–3 μM (Himmelheber et al. 2000; Pepeu and Giovannini 2004; Mattinson et al.

2011; Teles-Grilo Ruivo et al. 2017). In the neocortex, release of ACh occurs predominately via afferents originating from cholinergic neurons in the nucleus basalis of Meynert of the basal forebrain (Mesulam et al. 1983; Paul et al. 2015; Zaborszky et al. 2015); their terminals are densely distributed throughout all neocortical layers (Eckenstein et al. 1988; Henny and Jones 2008; Kalmbach et al. 2012). A classical view is that ACh invariably increases the excitability of excitatory neurons in neocortex (McCormick and Prince 1985; Mednikova et al. 1998; Desai and

Walcott 2006; Zhang and Seguela 2010; Hedrick and Waters 2015). However, a persistent hyperpolarization in layer 4 (L4) excitatory neurons was found in somatosensory cortex (Eggermann and Feldmeyer 2009; Dasgupta et al. 2018). This layer-specific cholinergic modulation may contribute to improving the cortical signal-to-noise ratio (SNR; Poorthuis et al. 2013; Obermayer et al. 2017; Radnikow and Feldmeyer 2018).

Although extensive studies have been conducted on the cholinergic modulation of neocortical excitatory neurons (Gil et al. 1997; Gulledge and Stuart 2005; Desai and Walcott 2006; Levy et al. 2006; Gulledge et al. 2007; Eggermann and Feldmeyer 2009), the action of ACh on the layer 6 (L6) microcircuitry has not been investigated systematically. Two main pyramidal cell (PC) classes exist in cortical L6, namely corticothalamic (CT) and corticocortical (CC) PCs. These two neuron types differ in their axonal projection patterns, dendritic morphological features, electrophysiological properties, and expression of molecular markers (Zhang and Deschenes 1997; Kumar and Ohana 2008; Thomson 2010; Pichon et al. 2012; Sundberg et al. 2018). CC PCs send intracortical projections mainly within the infragranular layers (Thomson 2010); CT PCs, in contrast, have few axons distributed in cortex and send projections directly back to the thalamus, thereby contributing to a feedback control of sensory input (Beierlein and Connors 2002; Lubke and Feldmeyer 2007; Oberlaender et al. 2012; Constantinople and Bruno 2013; Yang et al. 2014). The question how the function of these two classes of L6 PCs is modulated by ACh has so far not been explored.

Recent optogenetic studies suggest that PCs in L5 and L6 receive direct cholinergic synaptic input (Hedrick and Water 2015; Hay et al. 2016). In these neurons, ACh induces a slowly desensitizing inward current (I_{in}) in L6 PCs of prefrontal cortex through activation of $\alpha_4\beta_2$ subunit containing synaptic nicotinic ACh receptors (nAChRs; Kassam et al. 2008; Alves et al. 2010; Bailey et al. 2012; Poorthuis et al. 2013; Hay et al. 2016). However, there are very few studies focusing on the effects of muscarinic ACh receptors (mAChRs) in layer 6A (L6A) neurons (Tian et al. 2014; Sundberg et al. 2018). Here, using single and paired patch-clamp recordings with simultaneous biocytin filling, we investigated both muscarinic and nicotinic modulation of morphologically identified excitatory neurons and their synaptic connections in L6A of rat primary somatosensory barrel cortex. We found that ACh shows a cell-type-specific effect on both cellular and synaptic properties in L6A excitatory microcircuits through activation of mAChRs and/or nAChRs. Our results reveal that two functionally and morphologically distinct subpopulations of L6A PCs, CC and CT PCs, are differentially modulated by ACh. We demonstrate that ACh suppresses intracortical synaptic transmission via somatodendritic hyperpolarization and inhibition of presynaptic neurotransmitter release of CC PCs by activating M_4 mAChR subtype (M_4Rs). In contrast, CT PC shows a dual cholinergic modulation: These neurons are depolarized via M_1 mAChRs and $\alpha_4\beta_2$ subunit-containing nAChRs, while the presynaptic release probability is enhanced by $\alpha_4\beta_2$ nAChRs. In this way, ACh contributes to a facilitation of CT feedback.

Materials and Methods

Slice Preparation and Solutions for Electrophysiology

All experiments involving animals were performed in accordance with the EU Directive 2010/63/EU, the German animal welfare act, and the guidelines of the Federation of European Laboratory Animal Science Association (FELASA). Wistar rats

(Charles River) were maintained on a 12:12 h light:dark cycle from 7 AM to 7 PM. Rats aged 17–21 postnatal days (P17–21, of either sex) were lightly anesthetized with a concentration <0.1% of isoflurane and then decapitated. The brain was quickly removed and transferred into ice-cold artificial cerebrospinal fluid containing a high Mg^{2+} concentration and a low Ca^{2+} concentration (4 mM $MgCl_2$ and 1 mM $CaCl_2$) to reduce synaptic activity and bubbled continuously with carbogen (95% O_2 and 5% CO_2). It was then placed on the ramp of a slope of 10° and was cut at an angle of 50° to the midline. Thalamocortical slices were cut at 350 μm thickness using a high vibration frequency and incubated for 30–60 min at room temperature (21–24°C) in slicing solution. During whole-cell patch clamp recordings, slices were continuously perfused with a perfusion solution containing (in mM): 125 NaCl, 2.5 KCl, 25 D-glucose, 25 $NaHCO_3$, 1.25 NaH_2PO_4, 2 $CaCl_2$, 1 $MgCl_2$, 3 myo-inositol, 2 sodium pyruvate, and 0.4 ascorbic acid, bubbled with carbogen, and maintained at a temperature of 30–33°C. Patch pipettes were filled with an internal solution containing (in mM): 135 K gluconate, 4 KCl, 10 HEPES, 10 phosphocreatine, 4 Mg-ATP, and 0.3 GTP (pH 7.4, 290–300 mOsm). To stain the patched neurons, biocytin was added at a concentration between 3 and 5 mg/mL to the pipette solution; a recording time of ∼15–30 min was necessary for biocytin to diffuse into the dendrites and axons of the recorded cells (Marx et al. 2012; Qi et al. 2015). No biocytin was added to the internal solution of "searching" pipettes used during searching for synaptic connections.

Cell Identification

Slices were placed in the recording chamber under an upright microscope (fitted with 4× plan/0.13 numerical aperture and 40× water immersion/0.80 NA objectives; Olympus) with the pial surface pointing forward. The cortical layers and the barrel field were visualized at 4× magnification; the barrels can be identified in L4 as narrow dark stripes with evenly spaced, light "hollows" and were visible in 6–8 consecutive slices. L6A neurons were identified in the upper 60% of L6 at 40× magnification using infrared differential interference contrast microscope. Putative PCs and interneurons were differentiated on the basis of their intrinsic action potential (AP) firing pattern during recording and after histological processing by their morphological appearance.

Electrophysiological Recordings

Whole-cell patch clamp recordings from L6A neurons were performed at 30–33°C for an optimal oxygenation. Patch pipettes were pulled from thick-wall borosilicate capillaries (outer diameter: 2 mm; inner diameter: 1 mm) to a final resistance of 6–10 MΩ. Recordings were made using an EPC10 amplifier (HEKA), sampled at 10 kHz, and filtered at 2.9 kHz using the Patch-master software (HEKA). Neurons were selected randomly and excluded from the analysis when their whole-cell series resistance exceeded 40 MΩ (50 MΩ for neurons from paired recordings) or their resting membrane potential was more depolarized than −50 mV immediately after rupturing the cell membrane. The resting membrane potential of L6A excitatory neurons was continuously recorded in the current clamp mode to monitor changes in amplitude.

Miniature spontaneous events were recorded in voltage-clamp mode, and changes in mEPSC frequency and amplitude were analyzed. Recordings of L6A excitatory neurons were made

in the presence of tetrodotoxin (TTX; 0.5 μM) and gabazine (10 μM) to inhibit AP firing and inhibitory postsynaptic currents, respectively. During recordings, the holding potential was set at −70 mV.

Because the connectivity of L6A neurons was low compared with other intralaminar connections in rat barrel cortex, we followed the "searching procedure" described previously after patching a putative postsynaptic neuron (Qi et al. 2015). A monosynaptic connection can be found by patching multiple cells in "loose cell-attached" mode. When the AP resulted in a unitary excitatory postsynaptic potential (uEPSP) in the postsynaptic L6A neuron, this presynaptic neuron was repatched with a new pipette filled with biocytin containing internal solution. APs were elicited by current injection in the presynaptic neurons, and the postsynaptic response was recorded in whole cell (current clamp) mode, and the effects of ACh on uEPSPs were then tested.

Drug Application

ACh (1 μM–10 mM) was bath applied via the perfusion system or puff applied through a patch pipette (tip diameter: 1–2 μm) connected to a PDES-02D device (npi electronic GmbH). The puff pipette was placed at 10–20 μm from the same recorded neuron, and a brief low pressure was applied for about 1 s. Mecamylamine (10 μM), atropine (200 nM–20 μM), pirenzepine (0.5 μM), tropicamide (TRO, 1 μM), dihydro-ß-erythroidine (DHßE, 10 μM), methyllycaconitine (MLA, 10 μM), TTX (0.5 μM), and gabazine (10 μM) were all bath applied; drugs were purchased from Sigma-Aldrich or Tocris. The dose–response curve was fitted with the Hill equation by using the parameters E_{min}, E_{max}, E_{half}, and the Hill coefficient.

Histological Staining

After single cell or paired recordings, brain slices containing biocytin-filled neurons were processed as described previously (Marx et al. 2012). Slices were fixed at 4°C for at least 12 h in 100 mM phosphate buffer (PB, PH 7.4) solution containing 4% paraformaldehyde (PFA) and then incubated in 0.1% Triton X-100 solution containing avidin-biotinylated horseradish peroxidase (Vector ABC staining kit, Vector Laboratories, Inc.). The reaction was catalyzed using 3,3′-diaminobenzidine (Sigma-Aldrich) as a chromogen. Slices were again rinsed with 100 mM PB solution several times, followed by slow dehydration using ethanol and xylene. After embedding in Eukitt medium (Otto Kindler GmbH), the dendritic and axonal structures were clearly visible.

Immunofluorescence staining was performed for the identification of molecular markers expressed in L6A PCs. During electrophysiological recordings, Alexa Fluor 594 dye (1:500, Invitrogen) was added to the internal solution for post hoc identification of patched neurons. After recording, slices (350 μm) were fixed with 4% PFA in 100 mM phosphate buffered saline (PBS) for at least 24 h at 4°C and then permeabilized in 1% milk power solution containing 0.5% Triton X-100 and 100 mM PBS. Primary and secondary antibodies were diluted in the permeabilization solution (0.5% Triton X-100 and 100 mM PBS) shortly before experiments. For single-cell Fork-head box protein P2 (FoxP2) staining, slices were incubated overnight with Goat-anti-FoxP2 primary antibody (1:500, Santa Cruz Biotechnology) at 4°C and then rinsed thoroughly with 100 mM PBS. Subsequently, slices were treated with Alexa Fluor secondary antibodies (1:500) for 2–3 h at room temperature in the dark. After being rinsed in 100 mM PBS, the slices were embedded in Moviol. The fluorescence images were taken using the Olympus CellSens platform. The position of the patched neurons was identified by the conjugated Alexa dye, so that the expression of FoxP2 could be tested in biocytin-stained neurons. After acquiring fluorescent images, slices were incubated in 100 mM PBS overnight and were processed for subsequent morphological analysis. Coimmunostaining of FoxP2 and M_4Rs (Rabbit-anti-M_4Rs, 1:500, Abbexa) was performed with 150 μm thin brain slices following the procedure described above.

Morphological Reconstructions

3D reconstructions of L6A excitatory and inhibitory neurons or synaptically coupled neuron pairs labeled with biocytin were made using the NEUROLUCIDA software (MicroBrightField Inc.) and Olympus BX61 microscopy at 1000× magnification. Slices were selected to be reconstructed only if the labeling quality was high and the background staining was low. Barrel borders, demarcation of different layers, pial surface, and white matter were delineated during reconstructions. The cell body, the axonal and dendritic branches were reconstructed manually under constant visual inspection to detect even small collaterals. Corrections for shrinkage were performed in all spatial dimensions (factor 1.1 in the x and y axes, factor 2.1 in the z axis) (Marx et al. 2012). Analysis of 3D reconstructed neurons was done with NEUROEXPLORER software (MicroBrightField Inc.).

The neuronal polarity of reconstruction was calculated with NEUROEXPLORER software using cubic spline smoothing. The dendritic and axonal length was averaged for each of the 120 "3° sectors" around the soma. Data were recalculated and plotted in angular subdivisions around the soma, and polar plots were made with Grapher software (GoldenSoftware). The radian depicts degree in angles (°) with 0° toward the pial surface, 90° toward the posterior-median axis, 180° toward the white matter, and 270° toward the anterior–lateral axis.

Data Analysis

Custom written macros for Igor Pro 6 (WaveMetrics) were used to analyze the recorded electrophysiological signals. The miniature spontaneous activity was analyzed using the program SpAcAn (https://www.wavemetrics.com/project/SpAcAn). A threshold of 5 pA was set manually for detecting mEPSC events, which is at least 2.5-fold larger than the noise level (<2pA). No noise filtration was applied before data analysis.

The synaptic properties were evaluated as described in the previous studies (Feldmeyer et al. 1999). First, all sweeps were aligned to their corresponding presynaptic AP peaks, and an average sweep was generated as the mean uEPSP. The EPSP amplitude was calculated as the difference between the mean baseline amplitude and the maximum voltage of the postsynaptic event. The paired-pulse ratio (PPR) was defined as the second uPSP amplitude divided by the first uPSP amplitude of the mean uPSP elicited by paired APs with a stimulation frequency of 10 Hz. Failures were defined as events with amplitudes <1.5× the standard deviation (SD) of the noise within the baseline window, and the failure rate refers to the percentage of failures. The coefficient of variation (CV) was calculated as the SD divided by the mean uEPSP amplitude.

Statistical Tests

For all data, the mean $\pm$ SD was given. To assess the differences between two paired groups under different pharmacological conditions, Wilcoxon signed-rank test was performed. The paired Student's t-test was used when $n = 4$ for the paired samples, and the Mann–Whitney U test was used when the sample size was different between two groups. Statistical significance was set at $P < 0.05$, n indicates the number of neurons or pairs analyzed.

Results

ACh Either Depolarizes or Hyperpolarizes L6A PCs through Activation of mAChRs

Whole-cell patch clamp recordings from L6A neurons were performed in acute brain slices of rat barrel cortex with simultaneous biocytin fillings. During recordings, excitatory neurons were distinguished from interneurons by their regular firing pattern with a low maximum firing frequency. Following the bath application of 100 µM ACh, one subset of L6A PCs showed a membrane potential HP by on average -2.0 ± 1.0 mV ($n = 14$), whereas another was depolarized by $+9.5 \pm 6.1$ mV ($n = 15$; Fig. 1A). In addition, 1 s current pulses were injected in the recorded neuron to elicit AP firing before and during bath application of ACh. During the suprathreshold stimulus (100 pA above the rheobase current), the firing frequency was decreased by ACh in L6A PCs indicating an ACh-induced hyperpolarization but increased in PCs that exhibit a depolarizing ACh response (Fig. 1A,B). Notably, both ACh-induced hyperpolarization and depolarization were not transient but persisted until the end of bath application. For L2/3 and L5 PCs, it has been reported that the ACh-induced depolarization was preceded by an initial transient HP mediated by "small conductance," Ca^{2+}-activated K^+ channels (Gulledge and Stuart 2005; Gulledge and Kawaguchi 2007; Eggermann and Feldmeyer 2009; Dasari et al. 2017). For detecting the "fast" biphasic response, puff application of ACh was performed on L6A PCs. We were able to reproduce earlier findings in L2/3 and L5 PCs (Gulledge and Stuart 2005; Gulledge and Kawaguchi 2007; Eggermann and Feldmeyer 2009) under the same recording condition; however, ACh puff application onto L6A PCs always resulted in a monophonic M_1R-mediated response (Supplementary Figure 1).

To determine which fraction of the membrane potential changes in L6A pyramidal neurons is mediated by mAChRs, 20 µM atropine (ATRO, a general mAChR antagonist) was applied in voltage-clamp mode. Both the ACh-induced outward (I_{out}) and I_{in} currents were found to be strongly blocked by ATRO (20 µM; Fig. 1C,D), suggesting that both ACh response types in L6A excitatory neurons are almost exclusively mediated by mAChRs. We hypothesized that the $G_{i/o}$ protein-coupled M_4Rs mediates the hyperpolarizing effects, while the $G_{q/11}$ protein-coupled M_1 mAChR subtype (M_1Rs) is responsible for the DP induced by ACh application. To test this, puff application of ACh (100 µM) was performed in the presence and absence of the selective mAChR antagonists in the perfusion solution. In the presence of 1 µM TRO (a selective M_4R antagonist), the ACh-induced hyperpolarization was abolished (Fig. 1E,G). Conversely, the ACh-induced depolarization was blocked by 0.5 µM pirenzepine (PIR, a selective M_1R antagonist; Fig. 1F,H). These results indicate that the persistent hyperpolarization and depolarization induced by low concentrations of ACh are mediated exclusively by M_4Rs and M_1Rs, respectively.

The dose dependence of the muscarinic effects was investigated by bath application of increasing concentrations of ACh in the presence of 1 µM MEC (a general nAChR antagonist) and 0.5 µM TTX (0.3–300 µM; Fig. 1I,J). The dose–response curve was obtained by fitting the data to the Hill equation. For hyperpolarizing L6A PCs, the ACh concentration for a half-maximum response (EC_{50}) was 6.2 ± 1.3 µM, while for depolarizing neurons, the EC_{50} was 26.7 ± 5.4 µM. Thus, an ACh concentration of 30 µM was adopted for all subsequent experiments; this concentration resulted in a >50% of the maximum response in both subgroups of L6A excitatory neurons. In addition, when only 30 µM ACh was used, neurons did not respond with AP firing, which was occasionally observed when applying 100 µM ACh.

Cholinergic Responses in L6A PCs Are Cell-Type Specific

To investigate whether the two different cholinergic response types are specific for a defined L6A PC type, we characterized L6A PCs by their morphological, electrophysiological, and molecular features. Here, a total of 105 excitatory L6A neurons were recorded and morphologically reconstructed. Previous studies have consistently shown that CC and CT L6A PCs can be distinguished reliably by their axonal projection patterns (Zhang and Deschenes 1997; Mercer et al. 2005; Kumar and Ohana 2008; Pichon et al. 2012). Of all excitatory cells, 74 (70.5%) were identified as putative CT PCs, while 31 (29.5%) were putative CC PCs. CC L6A PCs displayed a dense horizontal axonal projection pattern in infragranular layers spanning several neighboring barrel columns; CT L6A PCs, on the other hand, showed a sparse columnar axonal domain with the majority of collaterals projecting directly toward the pial and terminating predominantly in L4 (cf. Fig. 2A). CC PCs have a significantly larger axonal length ($15\,523 \pm 5013$ vs. 5209 ± 1462 µm, $P < 0.001$) and horizontal axonal field span (1714 ± 350 vs. 358 ± 111 µm, $P < 0.001$) compared with CT PCs. Similar differences were also detected in the horizontal axonal and dendritic field span (1714 ± 350 vs. 358 ± 111 µm, $P < 0.001$ and 361 ± 58 vs. 232 ± 28 µm, $P < 0.001$, respectively, for CC vs. CT L6A PCs). For CC L6A PCs, these values are likely to be strong underestimates (by $\geq 90\%$, cf. Narayanan et al. 2015) because in acute brain slice preparations, long-range axonal collaterals will be severely truncated; however, this does not prevent an unambiguous cell-type identification. In addition, CC L6A PCs have more first-order axon collaterals ($P < 0.001$) but fewer dendrites ($P < 0.001$) than CT PCs (Fig. 2B). The features described above are reflected in the polar plots (Fig. 2A).

In addition, we determined the electrophysiological properties of morphologically identified CC ($n = 11$) and CT ($n = 9$) L6A PCs. Compared with CT PCs, CC PCs showed a significantly lower R_{in} ($P < 0.05$), a longer onset time ($P < 0.01$) for the first AP evoked by injecting a rheobase current and a longer AP half-width ($P < 0.05$). Trains of spikes were elicited to examine the firing behavior. The AP adaptation ratio (2:10 ISI) of CC PCs was smaller ($P < 0.05$) than that of CT cells because they exhibited an initial spike burst (Supplementary Figure 2). The differences in passive and active electrophysiological properties found here are in accordance with previous studies (Kumar and Ohana 2008; Tian et al. 2014).

Furthermore, the nuclear transcription factor FoxP2 is coexpressed with the neurotensin receptor 1 (NtsR1) gene, a molecular marker for CT L6A PCs in mice (Tasic et al. 2016; Sundberg et al. 2018). To identify the expression of FoxP2 in L6A
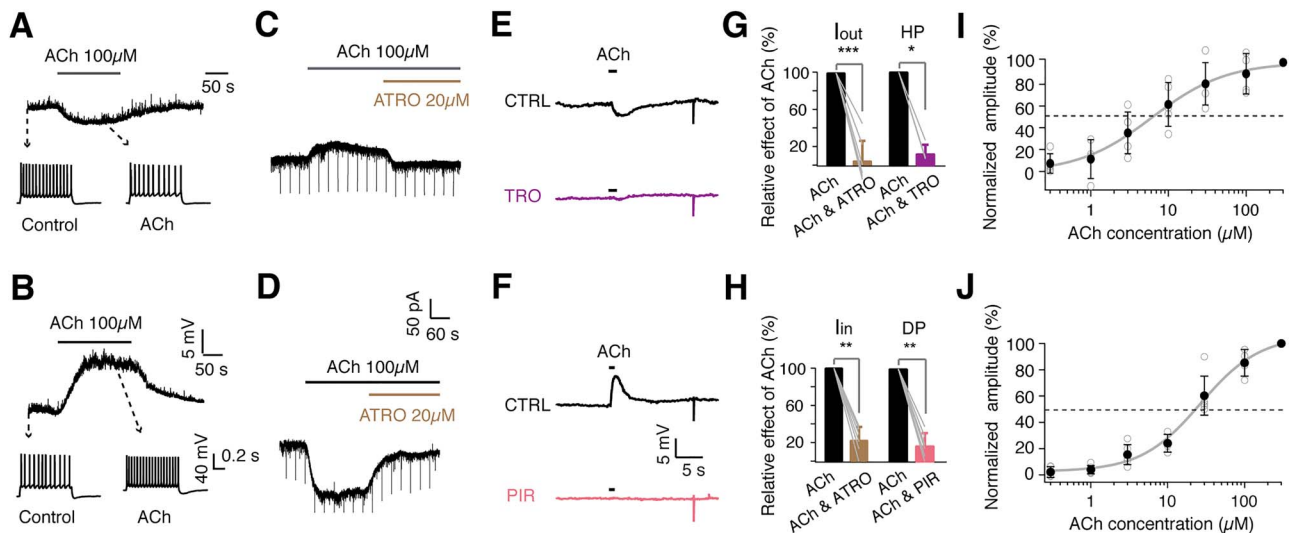
Figure 1. Low concentrations of ACh induce either a hyperpolarization or a depolarization of L6A PCs by activating mAChRs. (*A,B*) Top, L6A PC either shows a hyperpolarizing (*A*) or a depolarizing (*B*) response following the bath application of 100 μM ACh. Bottom, firing patterns of neurons in response to 1 s depolarizing current injection (rheobase +100 pA) before and during ACh application. (*C,D*) Representative voltage-clamp recordings with bath application of ACh showing I_{out} (*C*) or I_{in} (*D*) in L6A PCs. The effects are blocked by 20 μM ATRO. (*E,F*) Representative current-clamp recordings showing that puff application of ACh (100 μM) evokes a fast hyperpolarization (*E*) or depolarization (*F*) in L6A PCs. The specific M_1 mAChR antagonist PIR (0.5 μM) or the specific M_4 mAChR antagonist TRO (1 μM), respectively, were added to the perfusion solution to block ACh-induced membrane potential changes. (*G,H*) Summary bar graphs showing the percentage block by general and specific mAChR antagonists. $n = 7$, $P = 0.0006$ for I_{out} group, $n = 7$, $P = 0.0022$ for I_{in} group, $n = 4$, $P = 0.029$ for hyperpolarization group, and $n = 6$, $P = 0.0022$ for depolarization group. Statistical analysis was performed using the Mann–Whitney U test. Error bars represent SD. (*I,J*) Muscarinic responses of ACh were examined in the presence of 1 μM MEC and 0.5 μM TTX via bath applying ACh. ACh dose–response curves for hyperpolarizing ($n = 5$) (*I*) and depolarizing ($n = 8$) (*J*) L6A PCs are fitted by the Hill equation. Dashed lines represent half-maximal effects. The corresponding EC_{50} is 6.2 ± 1.3 μM for hyperpolarizing PCs and 26.7 ± 5.4 μM for depolarizing PCs. Filled circles represent mean values of different ACh concentrations.

PCs, we performed whole-cell recordings with simultaneous filling of biocytin and fluorescent Alexa Fluor 594 dye ($n = 14$). Subsequently, brain slices were processed for FoxP2 immunofluorescence staining. We found that CT L6A PCs were FoxP2-positive, while CC PCs are FoxP2-negative (Supplementary Figure 3A,B). The tight correlation between neuronal morphology, electrophysiology, and FoxP2 expression demonstrates the reliability of classification based on axonal projection patterns of CC and CT PCs.

ACh at a concentration of 30 μM was bath applied to 63 morphological identified L6A neurons. CC L6A PCs showed a hyperpolarizing response with a mean amplitude of -1.76 ± 4.28 mV (from -61.9 ± 5.6 to -63.6 ± 7.0 mV; $P < 0.05$, $n = 35$). In contrast, ACh (30 μM) induced a strong depolarization with a mean amplitude of $+11.4 \pm 4.6$ mV (from -70.3 ± 5.1 to -58.8 ± 7.4 mV; $P < 0.001$, $n = 14$) in CT PCs without exception (Fig. 2C). In Fig. 2D, ACh-induced membrane potential changes are plotted against the horizontal axonal field span revealing a strong correlation between axonal morphology and cholinergic response for the two L6A PC types. In addition, by performing immunostaining, we confirmed that M_4Rs was enriched within L6A. We found that M_4R-positive neurons were FoxP2-negative, while virtually no FoxP2-positive neuron expressed M_4Rs (Supplementary Figure 3D). This is consistent with our pharmacological result that only FoxP2-negative CC PCs showed a M_4Rs-mediated HP following the ACh application (Supplementary Figure 3).

CT PCs Are Selectively Activated by High Concentrations of ACh via α4β2 nAChRs

As demonstrated above, the depolarizing and hyperpolarizing effects of ACh in L6A PCs can be attributed to the activation of M_1 and M_4 mAChRs, respectively (Fig. 1C,D). However, previous

studies have shown that ACh excites L6A excitatory neurons by activating nAChRs (Kassam et al. 2008; Bailey et al. 2012; Poorthuis et al. 2013 ; Hay et al. 2016). In order to investigate the functional role of nAChRs in L6A of rat barrel cortex, we perfused slices continuously with 200 nM ATRO. Under this condition, 30 μM ACh had no effect on both CC and CT PCs ($P > 0.05$ for CC cells, $n = 5$; $P > 0.05$ for CT cells, $n = 5$; Fig. 3A); application of 1 mM ACh, however, strongly depolarized CT PCs by 7.7 ± 3.0 mV ($P < 0.001$, $n = 12$), while CC PCs showed no response ($P > 0.05$, $n = 5$; Fig. 3B). Our results demonstrate that both the muscarinic and nicotinic modulation of L6A PCs are cell-type specific; nAChRs are present solely in CT L6A PCs and activated substantially only by high ACh concentrations. To determine the concentration range in which ACh activates postsynaptic nAChRs, we measured the dose–response curve for ACh in the presence of 200 nM ATRO. A fit of dose–response relationship to the Hill equation gave an EC_{50} of 1.2 ± 0.3 mM ($n = 5$) for the nicotinic ACh response (Fig. 3C), a value more than about two orders of magnitude larger than those of the de- and hyperpolarizing muscarinic response.

It has been reported that the expression of nAChR subtypes in the neocortex exhibits layer specificity. L6A PCs in prefrontal cortex show a slow I_{in} to ACh by activating nAChRs containing the α_4 and β_2 subunits (Poorthuis et al. 2013; Hay et al. 2016). To confirm that this nAChR subtype mediates the response, the response of CT L6A PCs to application of 1 mM ACh was recorded in an ATRO-containing perfusion solution. In the presence of DHßE (10 μM), a nicotinic antagonist specific for $\alpha_4\beta_2*$ nAChRs, the ACh-dependent DP in CT PCs was eliminated, suggesting that CT L6A PCs express postsynaptic $\alpha_4\beta_2$ subunit-containing nAChRs (Fig. 3D). This is in accordance with the previous histochemical and optogenetic studies that have demonstrated the presence of $\alpha_4\beta_2*$ nAChR in neocortical L6 (Wada et al. 1989; Poorthuis et al. 2013).
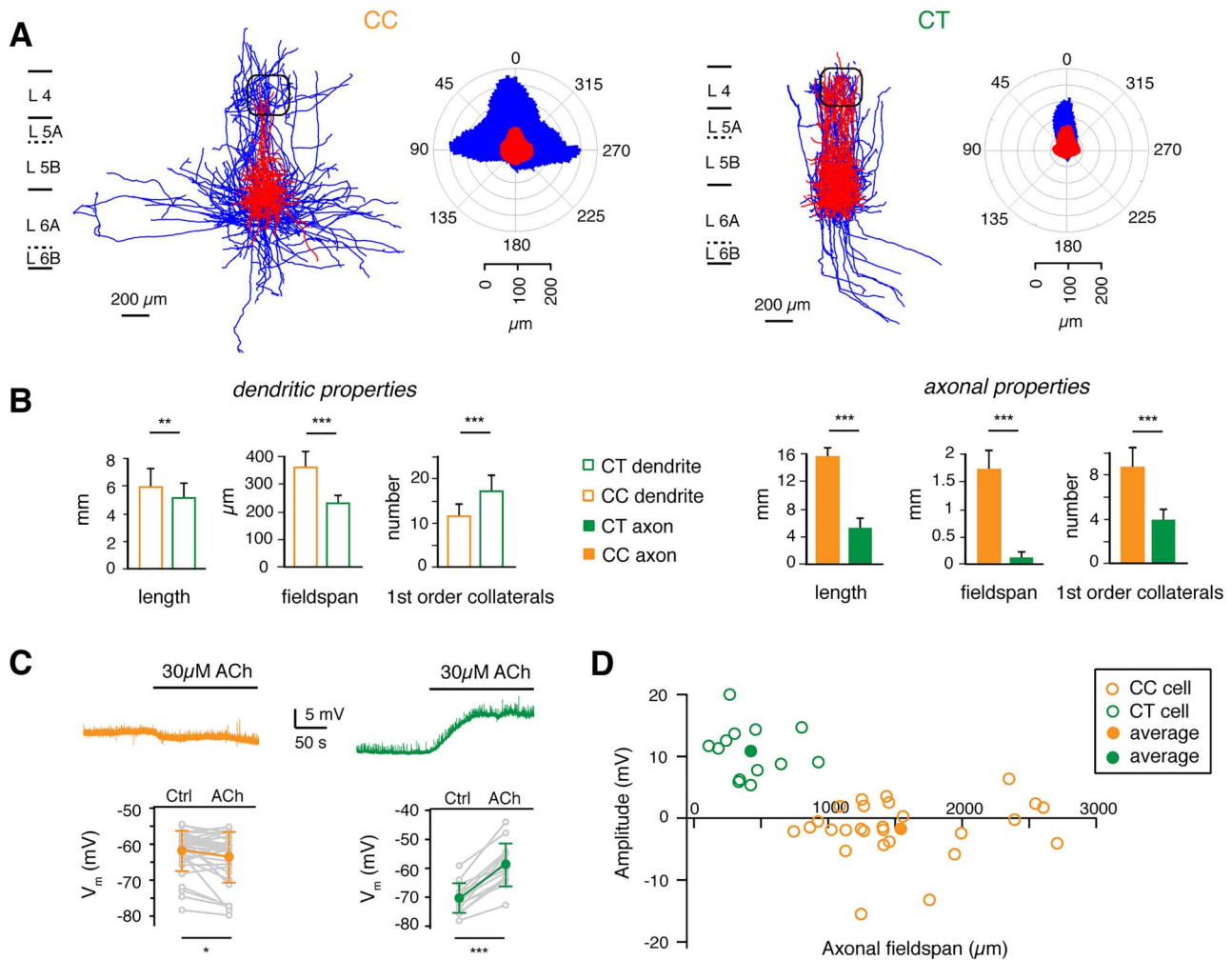
Figure 2. ACh hyperpolarizes CC L6A PCs but depolarizes CT L6A PCs. (A) Left, overlay of reconstructions of CC and CT PCs. Reconstructions of PCs were aligned with respect to the barrel center. Right, polar plots of CC and CT PCs. $n = 15$ for each group. Somatodendrites are shown in red, and axons are shown in blue. (B) Histograms comparing the length, field span, and number of first-order collaterals of axonal and dendritic structures for the two groups of PCs. $n = 21$ for CC neurons and $n = 54$ for CT neurons. Dendritic length: $P = 0.0015$, dendritic field span: $P = 1.4 \times 10^{-10}$, number of dendritic main nodes: $P = 1.7 \times 10^{-6}$; axonal length: $P = 9.6 \times 10^{-8}$, dendritic field span: $P = 4.8 \times 10^{-11}$, number of axonal main nodes: $P = 8.5 \times 10^{-11}$ for the Mann–Whitney U test. (C) Top, representative current-clamp recordings of a depolarizing CC (orange) and a hyperpolarizing CT PC (green) following the bath application of 30 μM ACh. Bottom, histograms of resting membrane potential (V_m) of L6A CC PCs in control and in the presence of 30 μM ACh ($n = 35$, $P = 0.019$ for Wilcoxon signed-rank test) and CT ($n = 14$, $P = 6.1 \times 10^{-5}$ for Wilcoxon signed-rank test) PCs. (D) Plots of the ACh-induced change in V_m versus axonal field span for two subtypes of PCs. Open orange circles, data from individual CC PCs ($n = 27$); open green circles, data from individual CT PCs ($n = 13$). Filled orange circle, average data from CC cells; filled green circle, average data from CT cells.

ACh Differentially Modulate Miniature Spontaneous Activity of CC and CT L6A PCs

In addition to changing the membrane properties and excitability of neurons, ACh is also a powerful modulator of neurotransmitter release. Therefore, we measured the amplitude and frequency of miniature spontaneous activity by performing whole-cell voltage-clamp recordings from L6A PCs. The membrane potential was held at −70 mV, and inward miniature EPSCs (mEPSCs) were recorded in the presence of TTX (0.5 μM) and gabazine (10 μM).

We found that ACh differentially modulates miniature spontaneous activity in both L6A CC and CT PCs. The frequency but not the amplitude of mEPSCs in CC L6A PCs decreased significantly in the presence of 30 μM ACh (2.8 ± 0.8 vs. 2.2 ± 1.0 Hz; $n = 7$, $P < 0.01$), an effect that was blocked by the M_4Rs antagonist TRO (2.2 ± 1.0 vs. 2.8 ± 1.0 Hz; $n = 7$, $P < 0.01$) (Fig. 4A–C).

This suggests that ACh decreases the neurotransmitter release probability at synapses with CC L6A PCs via presynaptic M_4Rs. Similarly, when DHßE was coappled with TRO and ACh, a reduction of mEPSC frequency without a change in mEPSC amplitude was observed (Supplementary Figure 4). This implies that in addition to M_4Rs, $\alpha_4\beta_2$ nAChRs also play a role in the cholinergic modulation of excitatory synaptic transmission onto CC PCs.

In contrast to CC L6A PCs, application of 30 μM ACh significantly decreased the interevent interval of mEPSCs in CT PCs, reflecting an increase in mEPSC frequency (0.95 ± 0.36 vs. 2.12 ± 0.68 Hz; $n = 7$, $P < 0.01$), while the mEPSc amplitude remained unaffected. Because ATRO did not affect the mEPSC frequency, we argued that the cholinergic effects on spontaneous mEPSCs in CT L6A PCs were not mediated by mAChRs but exclusively by presynaptic nAChRs. To test this, 10 μM DHßE was coappled with ACh. In the presence of DHßE, the ACh-induced
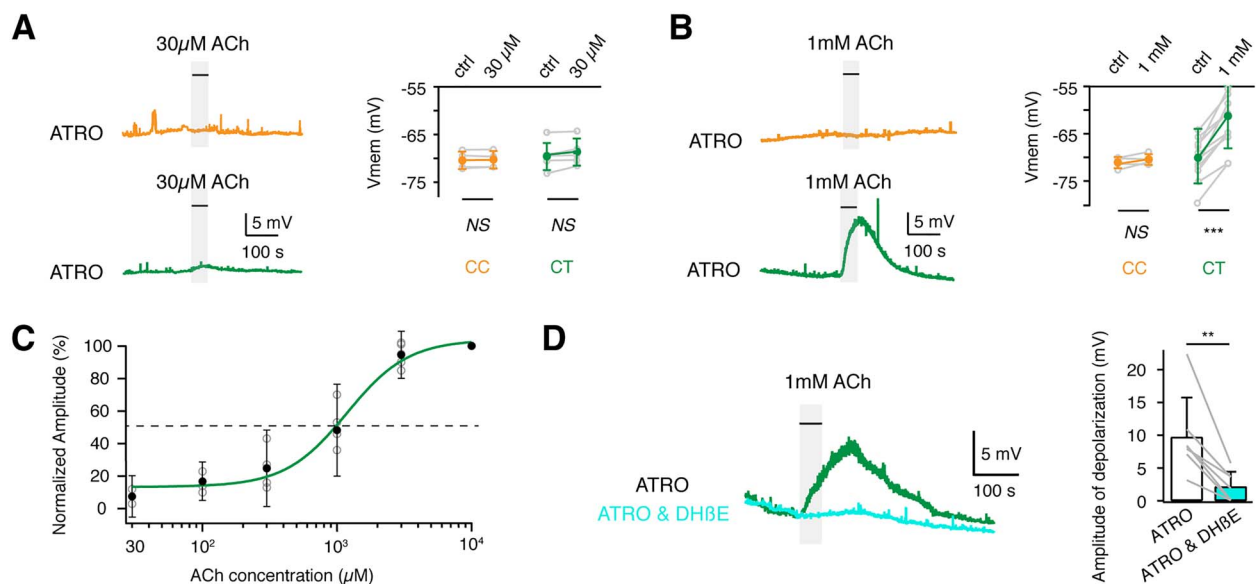
Figure 3. High concentration of ACh selectively depolarizes CT PCs. (A) In the presence of 200 nM ATRO, bath application of low concentration ACh (30 μM, 50 s) shows no effect on either CC (top) or CT (bottom) PCs. Summary plots show the resting membrane potential (V_m) under control and ACh conditions in L6A CC ($n = 5$, $P = 0.188$) and CT ($n = 5$, $P = 0.0625$) PCs. NS (not significant) for Wilcoxon signed-rank test. Error bars represent SD. (B) In the presence of 200 nM ATRO, bath application of 1 mM ACh for 50 s has no effect on CC L6A PCs (top) but induces a strong DP of CT L6A PCs (bottom). Summary plots showing V_m of CC L6A PCs under control conditions and in the presence of ACh in L6A CC ($n = 5$, $P = 0.156$) and CT ($n = 12$, $P = 0.0002$) PCs. Statistical analysis was performed using Wilcoxon signed-rank test. Error bars represent SD. (C) The dose–response curve of ACh under ATRO application (200 nM) in CT PCs ($n = 5$) is well fitted by the Hill equation. The dashed line indicates the half-maximal effect; the corresponding EC_{50} is 1.2 mM. Filled circles show mean effect of different concentrations, while open circles represent individual values. Error bars represent SD. (D) The DP induced by ACh bath application (in the presence of 200 nM ATRO) is blocked by 10 μM of the specific antagonist of $\alpha_4\beta_2$ subunit-containing nAChRs DHβE in CT L6A PCs. Summary plots showing the amplitude of the depolarization in response to application of 1 mM ACh in the presence of ATRO alone (open bar) and ATRO together with DHβE ($n = 7$, $P = 0.0078$ for Wilcoxon signed-rank test). Error bars represent SD.

increase of mEPSCs frequency in CT L6A PCs was reduced to control level (2.12 ± 0.68 vs. 1.01 ± 0.55; $n = 7$, $P < 0.05$; Fig. 4D–F). These results suggest that ACh potentiates excitatory synaptic transmission onto L6A CT PCs exclusively via presynaptic $\alpha_4\beta_2$ subunit containing nAChRs.

ACh Induces a Reduction of Presynaptic Neurotransmitter Release in CC L6A PCs but an Increase in CT PCs

To elucidate cholinergic effects on L6A PCs at pre- and postsynaptic sites independently, paired recordings and simultaneous biocytin fillings of synaptically coupled L6A neurons were performed. Excitatory neurons were classified as either CT or CC PCs based on the criteria mentioned above. During recordings, inhibitory interneurons were preliminarily identified by their high frequency AP firing pattern. After reconstructions, interneurons were further distinguished based on morphological features such as lack of dendritic spines. Thirty-four excitatory connections were established by presynaptic CC PCs. We found that ACh suppresses the synaptic efficacy of neuronal connections established by presynaptic CC PCs regardless of the postsynaptic neuron type (Fig. 5). The uEPSP amplitude of all synaptic connections with a presynaptic L6A CC PC was all significantly decreased by ACh (30 μM). For CC–CC connections, the uEPSP amplitude decreased from 0.45 ± 0.32 to 0.19 ± 0.14 mV ($n = 20$ pairs, $P < 0.001$), and for CC–CT connections, it changed from 0.35 ± 0.22 to 0.19 ± 0.13 mV ($n = 5$ pairs, $P < 0.05$). For CC–interneuron connections, the mean uEPSP was reduced from 0.90 ± 0.90 to 0.52 ± 0.58 mV ($n = 9$ pairs, $P < 0.05$) in the presence of ACh. ACh also significantly increased the PPR of

CC–CC (1.0 ± 0.4 vs. 1.5 ± 0.7, $P < 0.01$), CC–CT (1.2 ± 0.7 vs. 2.1 ± 1.6, $P < 0.05$), and CC–interneuron (1.0 ± 0.5 vs. 1.2 ± 0.5, $P < 0.01$) connections. Following the ACh application, CC–CC connections and CC–interneuron connections showed an increase in the CV; at CC–interneuron connections, the failure rate was also significantly increased (Fig. 5E; Supplementary Table 1). These changes in the EPSP properties suggest that ACh decreases the neurotransmitter release probability of intralaminar connections established by a presynaptic L6A CC PC. Other synaptic properties, like rise time, latency, and decay time, were not affected by ACh (Supplementary Table 1).

Because of their sparse and narrow axonal domain, L6A CT PCs rarely innervate neurons in their home layer and their intracortical synaptic connections are remarkably weak and unreliable (Mercer et al. 2005; West et al. 2006; Crandall et al. 2017). Here we applied ACh (30 μM) to seven synaptic connections established by a presynaptic CT PC in L6A, including two CT–CT, one CT–CC, and four CT–interneuron connections. In all synaptic connections established by CT PCs, ACh significantly enhanced the EPSP amplitude (0.10 ± 0.08 vs. 0.15 ± 0.10 mV; $n = 7$ pairs, $P < 0.05$) and reduced the PPR (3.0 ± 1.7 vs. 0.8 ± 0.6; $n = 7$ pairs, $P < 0.05$; Fig. 6). The ACh-mediated reduction in the PPR suggests a presynaptic locus for synaptic modulation. Because these connections display very small uEPSP amplitudes and frequent failures, the SNR was often too low to provide reliable estimates of the CV and failure rate. No significant differences were detected in rise time, decay time, and latency (Supplementary Table 1). Our findings indicate that in contrast to the inhibition of presynaptic release in L6A CC PCs, ACh enhances the synaptic efficacy of the weak connections established by a presynaptic CT PC.
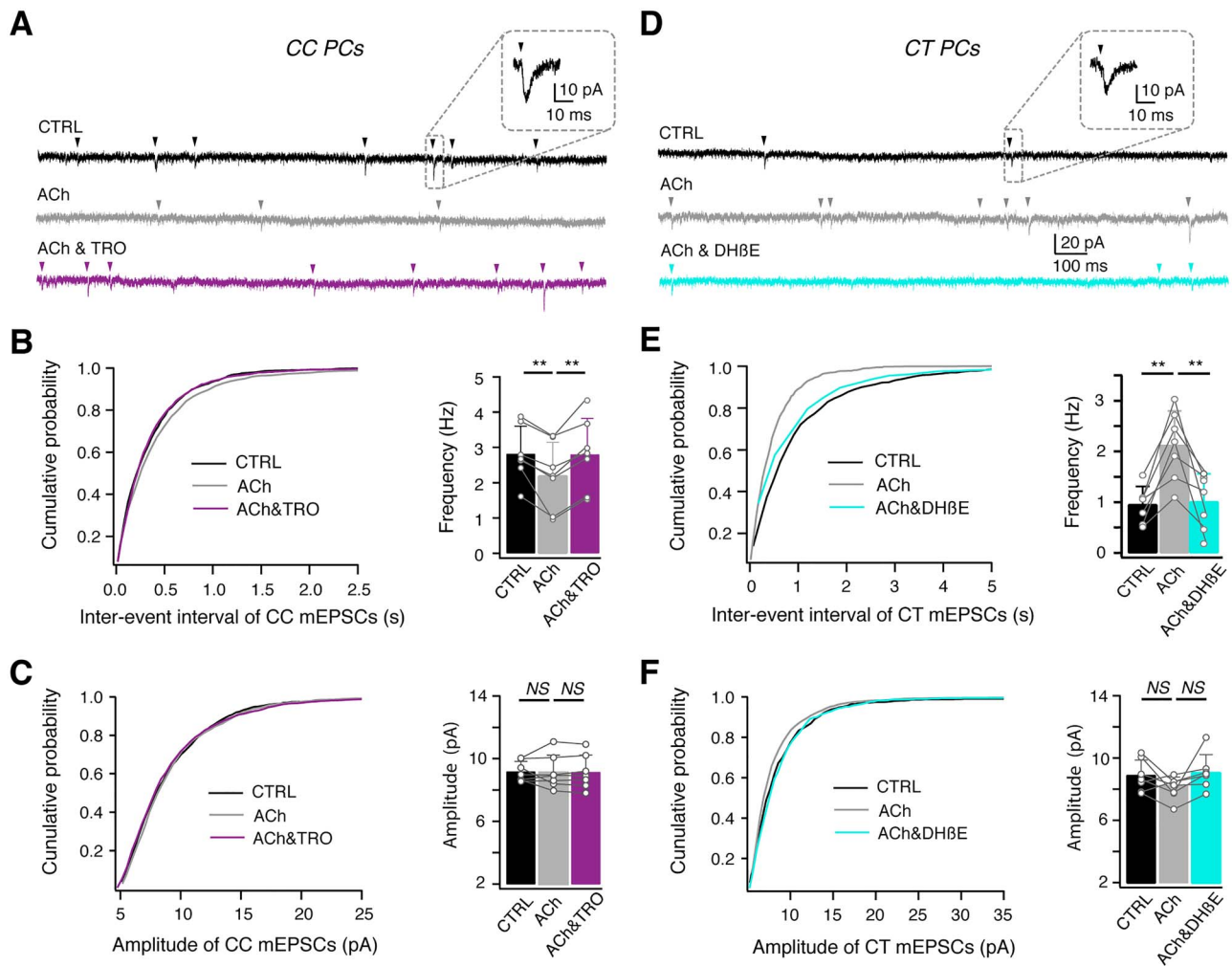
Figure 4. ACh differentially modulates miniature spontaneous activity in CC and CT L6A PCs. (A) Example voltage-clamp recordings of a CC L6A PCs under control (black), bath application of 30 µM ACh (gray), and coapplication of ACh and 1 µM TRO (purple). Miniature EPSCs were recorded in the presence of TTX (0.5 µM) and GABAzine (10 µM) at a holding potential of −70 mV. (B) Cumulative distributions of mEPSCs interevent interval recorded in CC L6A PCs under control condition, in the presence of ACh alone, and of ACh and TRO. Summary histograms of mEPSC frequency are shown on the right. ∗∗$P < 0.01$ for Wilcoxon signed-rank test. Error bars represent SD. (C) Cumulative distributions of mEPSCs amplitude recorded in CC L6A PCs under control, ACh, and ACh and TRO conditions. Summary histograms of mEPSC amplitude are shown on the right. Control versus ACh, $P = 0.8125$; ACh versus ACh and TRO, $P = 0.9375$, $n = 7$ for Wilcoxon signed-rank test. Error bars represent SD. (D) Example voltage-clamp recordings of a CT L6A PC in control (black), after bath application of 30 µM ACh (gray) and subsequent coapplication of ACh and 10 µM DHßE (turquoise). Miniature EPSCs were recorded in the presence of TTX (0.5 µM) and GABAzine (10 µM) at a holding potential of −70 mV. (E) Cumulative distributions of mEPSCs interevent interval recorded in CT L6A PCs under control, ACh, and ACh and DHßE conditions. Summary histograms of mEPSC frequency are shown on the right. ∗∗$P < 0.01$ for Wilcoxon signed-rank test. Error bars represent SD. (F) Cumulative distributions of mEPSCs amplitude recorded in CT L6A PCs under control, ACh, and ACh and DHßE conditions. Summary histograms of mEPSC amplitude are shown on the right. Control versus ACh, $P = 0.4258$; ACh versus ACh and DHßE, $P = 0.0781$, $n = 7$ for Wilcoxon signed-rank test. Error bars represent SD.

Previous studies have shown that ACh may inhibit intracortical excitatory synaptic transmission at some synaptic connections through activation of presynaptic M_4 mAChRs (Gil et al. 1997; Levy et al. 2006; Eggermann and Feldmeyer 2009). To test whether the ACh-induced suppression of the efficacy of synaptic connections with a presynaptic CC L6A PC is mediated by M_4 mAChR activation, 1 µM TRO (a selective antagonist of M_4Rs) was coapplied with ACh (30 µM) following bath application of ACh alone. The effects of ACh on synaptic connections established by CC PCs ($n = 6$ pairs, comprising 2 CC–CC, 1 CC–CT, and 3 CC–interneuron connections) were completely blocked by TRO (Fig. 7A). The EPSP amplitude decreased from 1.0 ± 0.8

to 0.3 ± 0.2 mV during ACh application and fully recovered to 1.0 ± 0.8 mV during coapplication of ACh and TRO. Moreover, TRO also blocked the ACh effects on the CV (0.8 ± 0.2 for control vs. 0.9 ± 0.3 for ACh and TRO; $n = 6$ pairs, $P = 0.75$) and failure rate (27.0 ± 17.6% for control vs. 26.3 ± 19.6% for ACh and TRO; $n = 6$ pairs, $P = 1.00$; Fig. 7B). In addition to reversing the ACh-induced increase in the PPR, TRO increased the PPR of connections established by CC PCs. Coapplication of ACh and TRO resulted in a smaller PPR than control (1.1 ± 0.3 vs. 1.3 ± 0.4; $n = 6$ pairs, $P < 0.05$; Fig. 7B). In order to isolate the presynaptic effect of ACh on L6A intralaminar connections established by presynaptic CC PCs, a CC–CT synaptically coupled pair was
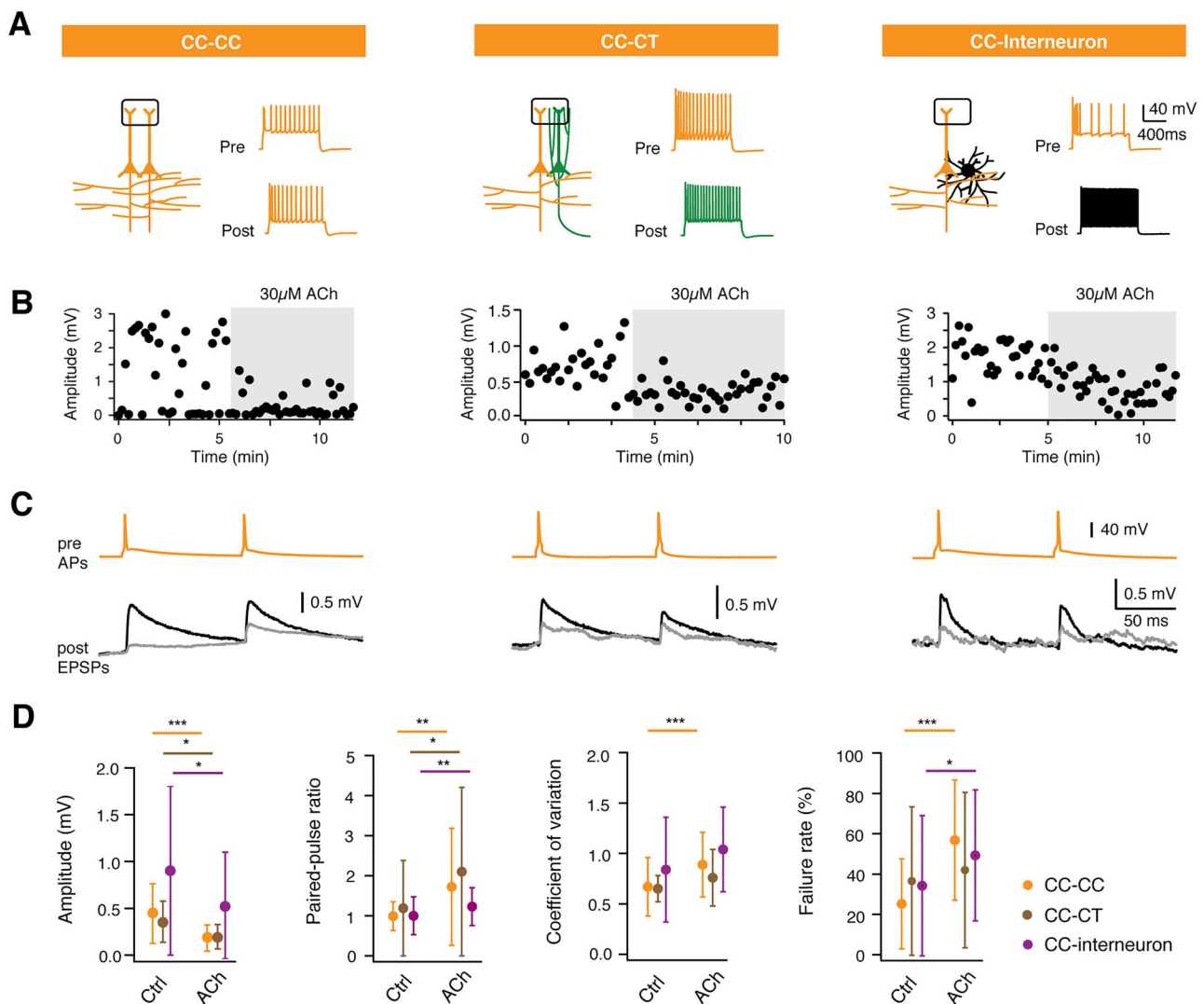
Figure 5. ACh-mediated reduction of presynaptic release at CC PC synapses. (A) Left, Schematic representation of the synaptic connections with a presynaptic CC L6A PC. CC PCs are shown in orange, the CT PC in green, and the interneuron in black. Barrel structures indicate L4. Right, corresponding firing patterns of pre- and postsynaptic neurons of the same connection type. (B) Time course of EPSP amplitude changes following the bath application of 30 μM ACh (gray phases) in a CC–CC, a CC–CT, and a CC–interneuron pair. (C) Overlay of average EPSPs in control (black) and ACh application (gray) phases. Presynaptic APs are shown at the top. Data are recorded from the same pairs as in (B). (D) The average and SD of several EPSP properties for CC–CC ($n = 20$), CC–CT ($n = 5$), and CC–interneuron ($n = 9$) connections are shown. $*P < 0.05$, $**P < 0.01$, $***P < 0.001$ for Wilcoxon signed-rank test.

recorded. The ACh-induced reduction in synaptic release probability recovered only after coapplication of TRO together with PIR but not when PIR (0.5 μM) was applied alone (Supplementary Figure 5).

To determine the AChR subtype that mediates the increase in synaptic efficacy at these connections, we tested whether the selective antagonists of M_1Rs (PIR), homomeric α_7 subunit-containing nAChRs (MLA), and heteromeric $\alpha_4\beta_2$ subunit-containing nAChRs (DHßE) could block the effect of ACh on synaptic connections with a presynaptic CT PC. While PIR and MLA had no effect, DHßE blocked the increase of EPSP amplitude and the decrease of PPR (Fig. 7C). This indicates that the ACh-induced enhancement of synaptic efficacy is induced by activation of $\alpha_4\beta_2$ subunit-containing nAChRs in presynaptic CT PCs.

Discussion

We investigated the cholinergic modulation of CT and CC PCs in L6A of the barrel cortex. We showed that 1) low concentrations of ACh differentially modulate the L6A microcircuitry by persistently depolarizing CT but hyperpolarizing CC L6A PCs. These effects are monophasic and mediated via M_1 and M_4 mAChRs, respectively; 2) a nicotinic ACh response was observed exclusively in CT PCs only when a high ACh concentration was applied. In addition, 3) low concentrations of ACh increase the frequency of mEPSCs via presynaptic nAChRs in L6A CT but decrease that of CC PCs via M_4Rs. To better understand the effects of ACh on intralaminar synaptic transmission, recordings were performed from synaptically coupled L6A PC pairs. We found that 4) in neuronal connections with a presynaptic CC PC, the neurotransmitter release probability was reduced via
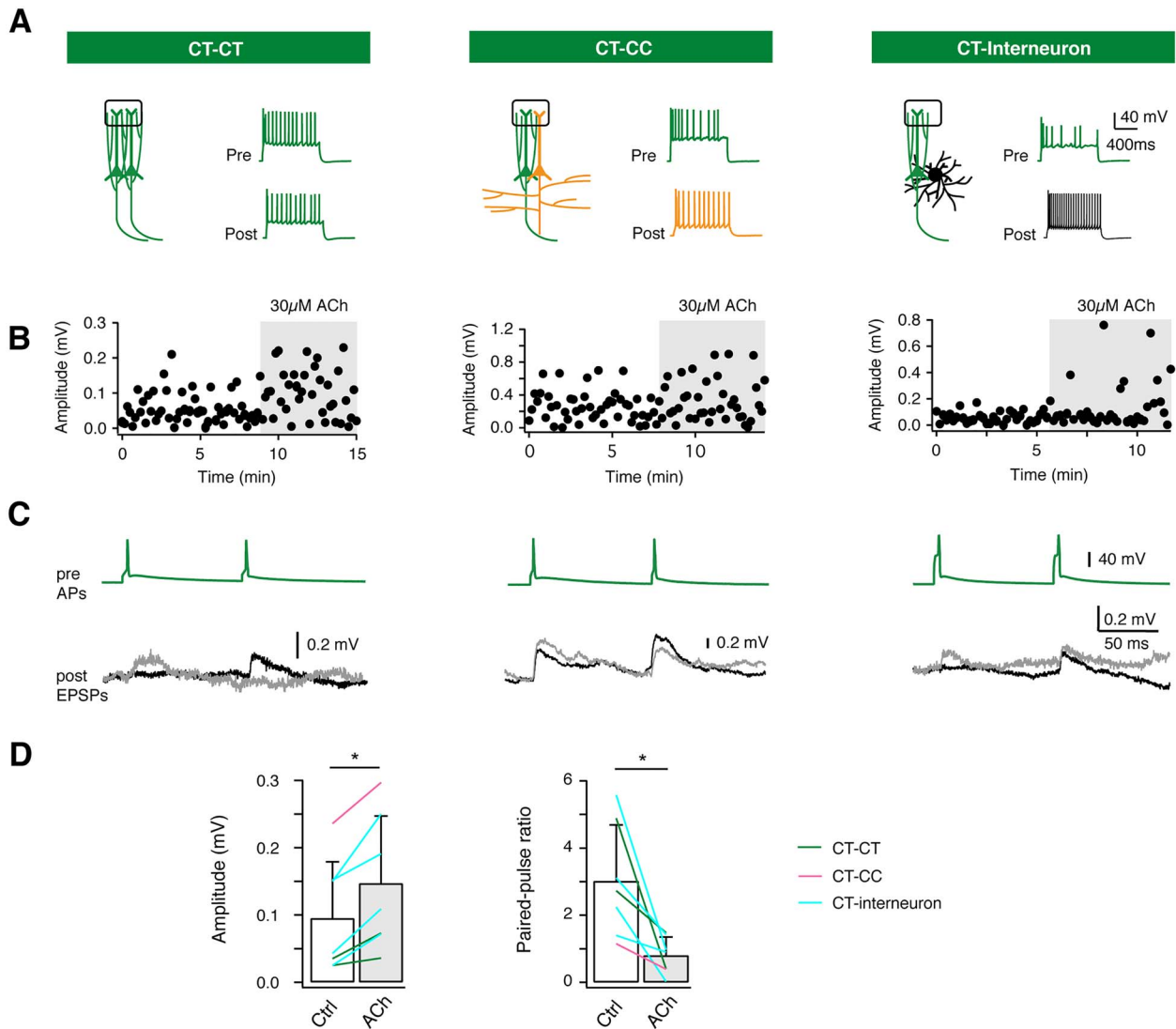
Figure 6. ACh enhances synaptic efficacy of L6A excitatory connections with a presynaptic CT PC. (A) Left, schematic representation of the synaptic connections with a presynaptic CT PC. Color code as in Fig. 5. Barrel structures indicate L4. Right, corresponding firing patterns of pre- and postsynaptic neurons of the same connection type. (B) Time course of EPSP amplitude changes following bath application of 30 μM ACh in a CT–CT, CT–CC, and CT–interneuron pair. (C) Overlay of average EPSPs in control (black) and ACh application (gray) phases. Presynaptic APs are shown at the top. Data are recorded from the same pairs as in (B). (D) Summary data ($n = 7$) of ACh-induced changes in first uEPSP amplitude and PPR for L6A excitatory pairs with a presynaptic CT L6A PC. Bars indicate the average for each condition; error bars represent SD. $*P < 0.05$ for Wilcoxon signed-rank test.

activation of M_4Rs but 5) increased in connections with a presynaptic CT L6A neuron by $\alpha_4\beta_2$ nAChR activation. Our results reveal that two functionally and morphologically distinct subpopulations of L6A PCs are affected differentially by ACh acting on both mAChRs and nAChRs.

Synergistic Modulation of L6A PCs by mAChRs and nAChRs

In a number of studies investigating the nAChR response of L6 PCs in different cortical areas, only high ACh concentrations (≥ 1 mM) have been applied because the ACh affinity of nAChRs is substantially lower than that of mAChRs (Kassam et al. 2008; Bailey et al. 2012; Poorthuis et al. 2013; Hay et al. 2016). Under this condition, any mAChR effect is almost entirely masked

by the strong nicotinic response, so that any involvement of mAChRs has been explicitly ruled out. Here we demonstrate for the first time that mAChRs play crucial roles in both pre- and postsynaptic modulation of L6 PC activity. Both the pre- and postsynaptic effects of mAChRs are already present at low ACh concentrations (1–10 μM) suggesting that neuromodulation via mAChRs is tonically present and mediated by volume transmission (Parikh et al. 2007; Sarter et al. 2009). In this study, the effect of endogenous ACh on presynaptic glutamate release of CC PCs was determined by coapplication of TRO and ACh (Fig. 7B). On the other hand, only a high concentration of ACh (EC_{50} of ~1 mM) could effectively depolarize CT L6A PCs via nAChRs, but an upregulation of presynaptic vesicle release via $\alpha_4\beta_2$ subunit-containing nAChRs was already observed in the presence of 30 μM ACh. This $\alpha_4\beta_2$ nAChR-mediated effect was
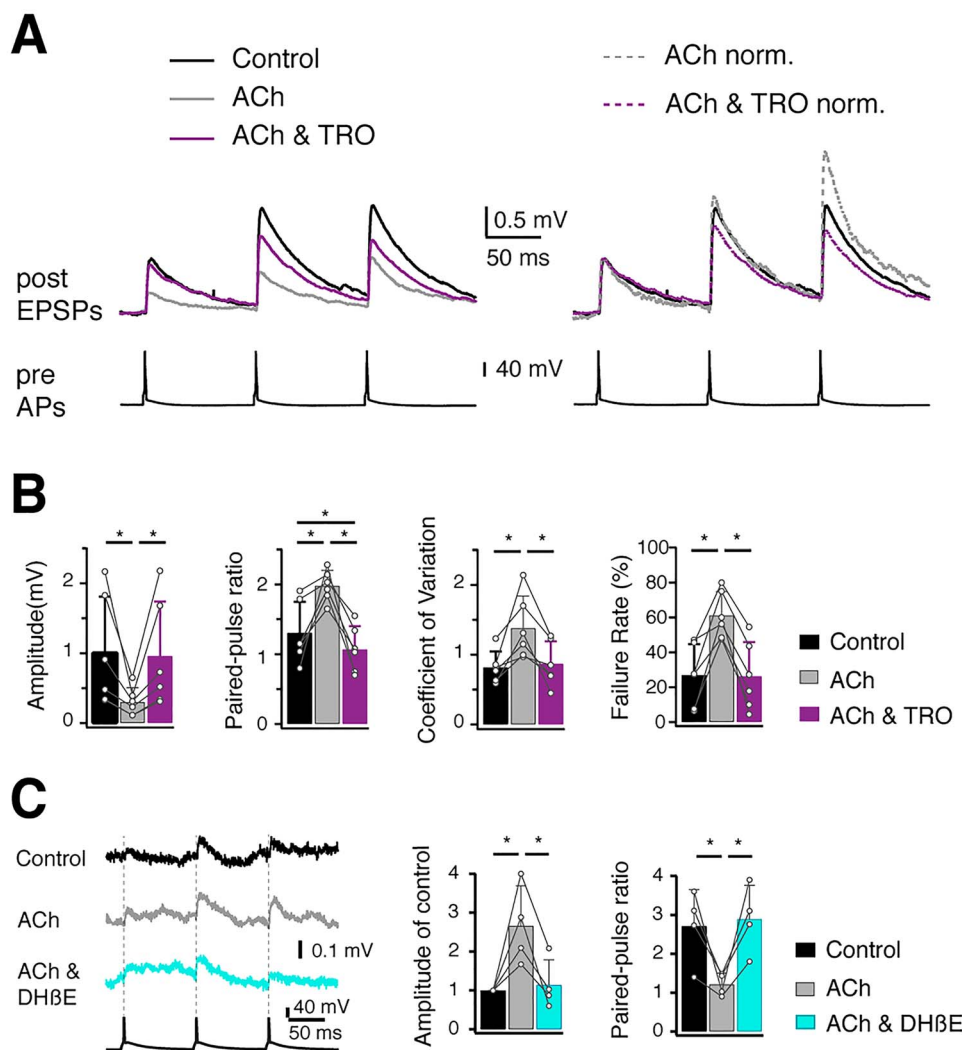
Figure 7. ACh decreases presynaptic release probability of CC PC via M_4 AChRs but increases that of CT PC via $\alpha_4\beta_2$ nAChRs. (A) Left, overlay of average EPSPs recorded in control, the presence of ACh (30 μM), and of ACh and TRO (1 μM) from a representative CC–CC connection. Right, normalizing the mean EPSP amplitudes obtained in ACh and ACh and TRO to the first EPSP amplitude in control reveals changes of PPR. Presynaptic APs are shown at the bottom. (B) Histograms ($n = 6$) showing the effect of ACh and TRO blockade of ACh-induced changes on several EPSP properties including EPSP amplitude, PPR, CV, and failure rate. Data were recorded from L6A synaptic connections with a presynaptic CC PC. Open circles, individual data points; bars, the average for each condition. Error bars represent SD. $*P < 0.05$ for Wilcoxon signed-rank test. (C) Left, average EPSPs recorded in control, the presence of ACh (30 μM) and of ACh and DHßE (10 μM) from a representative CT–CT connection. Gray phase, bath application of 30 μM ACh; turquoise phase, coapplication of ACh and DHßE. The presynaptic APs are shown at the bottom. Right, Histograms ($n = 4$) showing the effect of ACh and DHßE blockade of ACh-induced changes in first uEPSP amplitude and PPR. Data were recorded from L6A synaptic connections with a presynaptic CT PC. Open circles, individual data points; bars, the average for each condition. Error bars represent SD. $*P < 0.05$ for paired Student's t-test.

found for spontaneous excitatory synaptic activity as well as for CT-formed monosynaptic connections, suggesting that presynaptic nAChRs are expressed on synaptic boutons of both CT L6A axons and other glutamatergic afferents (e.g., from thalamus or other cortical regions). Single channel currents from nAChRs can be activated already by low concentrations of ACh (Colquhoun and Sakmann 1985; Mazzaferro et al. 2017). Because of the electronic compact structure of a presynaptic bouton, even the opening of a few nAChR receptor channels may result in a depolarization that is sufficiently strong to increase the open probability of presynaptic Ca^{2+} channels and hence the neurotransmitter release probability.

Furthermore, in some L6 PCs, the α_5 nAChR subunit coassembles with the α_4 and β_2 subunits (Poorthuis et al. 2013; Hay et al.

2016). Nicotinic AChRs containing the α_4, β_2 and α_5 subunits have a higher Ca^{2+} permeability than those composed of α_4 and β_2 nAChR subunits alone (Fucile 2004). In the presynaptic terminals, Ca^{2+} entry via $\alpha_4\beta_2\alpha_5$ nAChRs into the presynaptic bouton could enhance neurotransmitter release, providing that these channels are located sufficiently close to vesicle release site.

Cholinergic Activation by Endogenous ACh in Neocortical L6

Cholinergic signaling has been described to occur via a volume release mechanism (Sarter et al. 2009), which is slow and unspecific. Volume release of ACh reaches concentrations in a low micromolar range (Pepeu and Giovannini 2004;
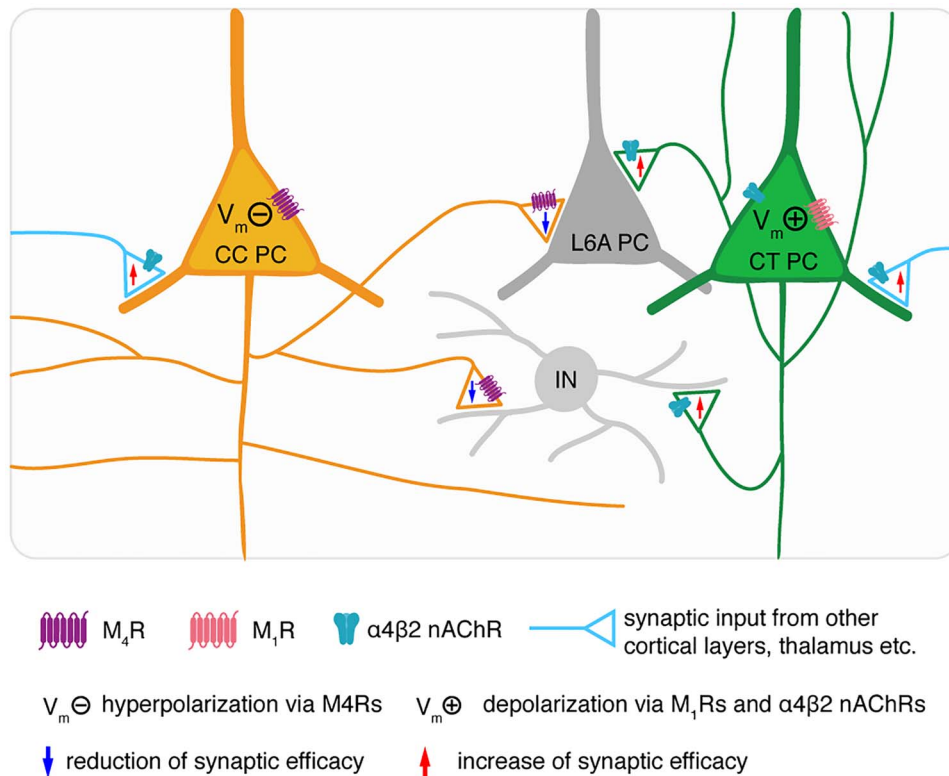
Figure 8. Cholinergic actions on muscarinic and nicotinic receptors in L6A PCs. Schematic summary shows cholinergic modulation of L6A microcircuits in rat barrel cortex. ACh affects membrane excitability and presynaptic release probability of L6A PCs via activating muscarinic and/or nicotinic AChRs. Because of the cell-type–specific distribution of AChRs at pre- and postsynaptic sites, CC and CT L6A PCs are affected differentially by ACh. The presynaptic CC and CT L6A PC are shown in orange and green, respectively. The postsynaptic L6A PC and interneuron are shown in gray.

Mattinson et al. 2011; Teles-Grilo Ruivo et al. 2017), spreads widely over neocortical layers, and activates predominantly mAChRs. In addition, cholinergic synapses have been identified particularly in deep layers of neocortex and less so in superficial cortical layers (Bennett et al. 2012; Hedrick and Waters 2015; Hay et al. 2016). At these cholinergic synapses, ACh reaches a high concentration in the synaptic cleft (Aidoo and Ward 2006), thereby activating postsynaptic nAChRs in L6 PCs (Hay et al. 2016). Because cholinergic synapses in the neocortex are small (Takacs et al. 2013), ACh released into the synaptic cleft may spill over into the perisynaptic space. Subsequently, extrasynaptic AChRs on presynaptic boutons of CT PCs are activated resulting in an increase in neurotransmitter release probability (Fig. 6). Thus, nAChRs and mAChRs act on different time scales and at different neurotransmitter concentrations, resulting in a striking complexity of the cholinergic modulation of neocortical signaling.

The Cell-Type–Specific Effect of ACh in L6A

ACh has been shown to induce a persistent DP of L2/3 and L5 PCs but a HP of excitatory L4 neurons (Gulledge et al. 2007; Eggermann and Feldmeyer 2009; Dasari et al. 2017). Here, we demonstrate that ACh modulates PCs not only in a layer-specific way but also a cell-type–specific way that can be attributed to a cell-type–dependent expression of mAChRs and nAChRs (Fig. 8). In L6A of barrel cortex, ACh hyperpolarizes CC PCs but depolarizes CT PCs via activation of M_4Rs and M_1Rs, respectively. The AP firing frequency was decreased by ACh in CC PCs but increased in CT PCs, thereby modulating the excitability and

signal propagation in L6A PCs in a cell-specific manner. In addition, CT L6A PCs but not CC PCs showed a strong $\alpha_4\beta_2$ nAChR-mediated response (Fig. 8). This is consistent with previous findings in L6 of prefrontal cortex that regular spiking neurons have a larger nicotinic receptor-mediated I_{in} following the ACh application when compared with bursting neurons (Kassam et al. 2008). A cell-type–specific neuromodulation was also discovered previously in deep layers of medial prefrontal cortex for neuromodulators such as noradrenaline, dopamine, and adenosine (Dembrow et al. 2010; van Aerde et al. 2015; Clarkson et al. 2017; Baker et al. 2018; Anastasiades et al. 2019).

By studying miniature spontaneous activity of L6A CC and CT PCs, we found that ACh both increases the excitatory synaptic release onto CC and CT PCs by activation of $\alpha_4\beta_2$ nAChRs (Fig. 8). Because CT PCs express $\alpha_4\beta_2$ nAChRs, an increase in spontaneous activity may result from the enhanced release probability at CT L6 PC boutons; however, the intracortical axon density of these PCs is low, so likely to be that their contribution to the spontaneous mEPSC frequency is minimal. On the other hand, activation of nAChRs increases thalamocortical transmission onto L3, L4, and L5 neocortical neurons (Gil et al. 1997; Lambe et al. 2003; Kawai et al. 2007). Thus, the increased excitatory transmission onto L6A PCs is probably resulting to a large degree from a higher release probability at thalamocortical and less so from intracortical synapses. In addition, CC PCs receive more intralaminar inputs than CT PCs, which can be suppressed by ACh via M_4Rs. Therefore, the ACh-induced reduction of mEPSC frequency in CC PCs could be a combinatorial effect on thalamocortical and intracortical transmission.

It has been proposed that ACh increases the SNR of sensory signaling by selectively enhancing thalamocortical inputs over intracortical synaptic transmission (Gil et al. 1997; Hsieh et al. 2000; Oldford and Castro-Alamancos 2003). ACh has been found to suppress the efficacy of excitatory intracortical connections in different layers including L2/3, L4, and L5 (Gil et al. 1997; Levy et al. 2006; Eggermann and Feldmeyer 2009). Here, a differential cholinergic modulation of presynaptic neurotransmitter release was observed in CC and CT L6A PC types. ACh suppresses synaptic transmission in excitatory L6A connections with presynaptic CC PCs through activation of M_4Rs but potentiates connections with a presynaptic CT PCs via presynaptic $\alpha_4\beta_2$ nAChRs (Fig. 8); no α_7 nAChR or M_1R effect on synaptic transmission was observed.

In hippocampus and some subcortical structures such as the ventral tegmental area, glutamatergic synapses are known to be facilitated by nAChRs located on presynaptic terminals (Gray et al. 1996; Mansvelder and McGehee 2000). However, very few studies demonstrate an ACh-mediated enhancement of intracortical excitatory synaptic transmission. Recently, it has been shown that excitatory synaptic transmission between PCs and somatostatin-positive interneurons in layer 2 of mouse barrel cortex is increased by ACh via activating nAChRs (Urban–Ciecko et al. 2018). Although an increase in synaptic efficacy was observed in connections with a presynaptic CT PCs, this type of synaptic connections is rare, generally weak, and very unreliable (West et al. 2006; Crandall et al. 2017). Therefore, we propose that ACh mainly acts on CT PCs not primarily by increasing intracortical synaptic transmission but rather by facilitating corticothalamocortical feedback; this facilitation will occur already at ACh levels in the low micromolar range.

In the neocortex, ACh levels change dramatically during different behavioral states such as sleep, awakening, arousal, and attention (Himmelheber et al. 2000; Teles-Grilo Ruivo et al. 2017). It has been suggested that high ACh levels serve to enhance the response to sensory stimuli by increasing the strength of afferent input, while low concentration of ACh contributes to the consolidation of encoded information (Hasselmo and McGaughy 2004). In this study, we clearly demonstrate that ACh suppresses intracortical synaptic transmission while increasing thalamocortical feedback via a cell-type–specific modulation of L6A PCs. This may contribute to maintaining a low internal noise level within the cortical circuits, thereby improving the "SNR" in sensory processing. In addition, ACh markedly affects the dynamics of the thalamocortical feedback loop by modulating the output of CT PCs. The thalamocortical feedback loop may serve in sharpening the spatial response properties of thalamic neurons and enhance the sensitivity to the sensory signals from the periphery (Krupa et al. 1999; Sillito and Jones 2002). This implies an important functional role of the L6 network during different behavioral stages. Our finding might lead to a better understanding of the mechanisms of interactions between the cholinergic system and behavioral signals, such as bottom-up and top-down attention (Avery et al. 2014; Ramaswamy et al. 2018).

Supplementary Material

Supplementary material is available at *Cerebral Cortex* online.

Funding

Notes

References

Aidoo AY, Ward K. 2006. Spatio-temporal concentration of acetylcholine in vertebrate synaptic cleft. *Math Comput Model.* 44:952–962.

Alves NC, Bailey CD, Nashmi R, Lambe EK. 2010. Developmental sex differences in nicotinic currents of prefrontal layer VI neurons in mice and rats. *PLoS One.* 5:e9261.

Anastasiades PG, Boada C, Carter AG. 2019. Cell-type-specific D1 dopamine receptor modulation of projection neurons and interneurons in the prefrontal cortex. *Cereb Cortex.* 29:3224–3242.

Avery MC, Dutt N, Krichmar JL. 2014. Mechanisms underlying the basal forebrain enhancement of top-down and bottom-up attention. *Eur J Neurosci.* 39:852–865.

Bailey CD, Alves NC, Nashmi R, De Biasi M, Lambe EK. 2012. Nicotinic alpha5 subunits drive developmental changes in the activation and morphology of prefrontal cortex layer VI neurons. *Biol Psychiatry.* 71:120–128.

Baker AL, O'Toole RJ, Gulledge AT. 2018. Preferential cholinergic excitation of corticopontine neurons. *J Physiol.* 596:1659–1679.

Beierlein M, Connors BW. 2002. Short-term dynamics of thalamocortical and intracortical synapses onto layer 6 neurons in neocortex. *J Neurophysiol.* 88:1924–1932.

Bennett C, Arroyo S, Berns D, Hestrin S. 2012. Mechanisms generating dual-component nicotinic EPSCs in cortical interneurons. *J Neurosci.* 32:17287–17296.

Clarkson RL, Liptak AT, Gee SM, Sohal VS, Bender KJ. 2017. D3 receptors regulate excitability in a unique class of prefrontal pyramidal cells. *J Neurosci.* 37:5846–5860.

Colquhoun D, Sakmann B. 1985. Fast events in single-channel currents activated by acetylcholine and its analogues at the frog muscle end-plate. *J Physiol.* 369:501–557.

Constantinople CM, Bruno RM. 2013. Deep cortical layers are activated directly by thalamus. *Science.* 340:1591–1594.

Crandall SR, Patrick SL, Cruikshank SJ, Connors BW. 2017. Infrabarrels are layer 6 circuit modules in the barrel cortex that link long-range inputs and outputs. *Cell Rep.* 21:3065–3078.

Dasari S, Hill C, Gulledge AT. 2017. A unifying hypothesis for M1 muscarinic receptor signalling in pyramidal neurons. *J Physiol.* 595:1711–1723.

Dasgupta R, Seibt F, Beierlein M. 2018. Synaptic release of acetylcholine rapidly suppresses cortical activity by recruiting muscarinic receptors in layer 4. *J Neurosci.* 38:5338–5350.

Dembrow NC, Chitwood RA, Johnston D. 2010. Projection-specific neuromodulation of medial prefrontal cortex neurons. *J Neurosci.* 30:16922–16937.

Desai NS, Walcott EC. 2006. Synaptic bombardment modulates muscarinic effects in forelimb motor cortex. *J Neurosci.* 26:2215–2226.

Eckenstein FP, Baughman RW, Quinn J. 1988. An anatomical study of cholinergic innervation in rat cerebral cortex. *Neuroscience*. 25:457–474.

Eggermann E, Feldmeyer D. 2009. Cholinergic filtering in the recurrent excitatory microcircuit of cortical layer 4. *Proc Natl Acad Sci U S A*. 106:11753–11758.

Feldmeyer D, Egger V, Lubke J, Sakmann B. 1999. Reliable synaptic connections between pairs of excitatory layer 4 neurones within a single 'barrel' of developing rat somatosensory cortex. *J Physiol*. 521(Pt 1):169–190.

Fucile S. 2004. Ca2+ permeability of nicotinic acetylcholine receptors. *Cell Calcium*. 35:1–8.

Gil Z, Connors BW, Amitai Y. 1997. Differential regulation of neocortical synapses by neuromodulators and activity. *Neuron*. 19:679–686.

Gray R, Rajan AS, Radcliffe KA, Yakehiro M, Dani JA. 1996. Hippocampal synaptic transmission enhanced by low concentrations of nicotine. *Nature*. 383:713–716.

Gulledge AT, Kawaguchi Y. 2007. Phasic cholinergic signaling in the hippocampus: functional homology with the neocortex? *Hippocampus*. 17:327–332.

Gulledge AT, Park SB, Kawaguchi Y, Stuart GJ. 2007. Heterogeneity of phasic cholinergic signaling in neocortical neurons. *J Neurophysiol*. 97:2215–2229.

Gulledge AT, Stuart GJ. 2005. Cholinergic inhibition of neocortical pyramidal neurons. *J Neurosci*. 25:10308–10320.

Hasselmo ME. 2006. The role of acetylcholine in learning and memory. *Curr Opin Neurobiol*. 16:710–715.

Hasselmo ME, McGaughy J. 2004. High acetylcholine levels set circuit dynamics for attention and encoding and low acetylcholine levels set dynamics for consolidation. *Prog Brain Res*. 145:207–231.

Hasselmo ME, Sarter M. 2011. Modes and models of forebrain cholinergic neuromodulation of cognition. *Neuropsychopharmacology*. 36:52–73.

Hay YA, Lambolez B, Tricoire L. 2016. Nicotinic transmission onto layer 6 cortical neurons relies on synaptic activation of non-alpha7 receptors. *Cereb Cortex*. 26:2549–2562.

Hedrick T, Waters J. 2015. Acetylcholine excites neocortical pyramidal neurons via nicotinic receptors. *J Neurophysiol*. 113:2195–2209.

Henny P, Jones BE. 2008. Projections from basal forebrain to prefrontal cortex comprise cholinergic, GABAergic and glutamatergic inputs to pyramidal cells or interneurons. *Eur J Neurosci*. 27:654–670.

Herrero JL, Roberts MJ, Delicato LS, Gieselmann MA, Dayan P, Thiele A. 2008. Acetylcholine contributes through muscarinic receptors to attentional modulation in V1. *Nature*. 454:1110–1114.

Himmelheber AM, Sarter M, Bruno JP. 2000. Increases in cortical acetylcholine release during sustained attention performance in rats. *Brain Res Cogn Brain Res*. 9:313–325.

Hsieh CY, Cruikshank SJ, Metherate R. 2000. Differential modulation of auditory thalamocortical and intracortical synaptic transmission by cholinergic agonist. *Brain Res*. 880:51–64.

Jones BE. 2004. Activity, modulation and role of basal forebrain cholinergic neurons innervating the cerebral cortex. *Prog Brain Res*. 145:157–169.

Kalmbach A, Hedrick T, Waters J. 2012. Selective optogenetic stimulation of cholinergic axons in neocortex. *J Neurophysiol*. 107:2008–2019.

Kassam SM, Herman PM, Goodfellow NM, Alves NC, Lambe EK. 2008. Developmental excitation of corticothalamic neurons by nicotinic acetylcholine receptors. *J Neurosci*. 28:8756–8764.

Kawai H, Lazar R, Metherate R. 2007. Nicotinic control of axon excitability regulates thalamocortical transmission. *Nat Neurosci*. 10:1168–1175.

Krupa DJ, Ghazanfar AA, Nicolelis MA. 1999. Immediate thalamic sensory plasticity depends on corticothalamic feedback. *Proc Natl Acad Sci U S A*. 96:8200–8205.

Kumar P, Ohana O. 2008. Inter- and intralaminar subcircuits of excitatory and inhibitory neurons in layer 6A of the rat barrel cortex. *J Neurophysiol*. 100:1909–1922.

Lambe EK, Picciotto MR, Aghajanian GK. 2003. Nicotine induces glutamate release from thalamocortical terminals in prefrontal cortex. *Neuropsychopharmacology*. 28:216–225.

Levy RB, Reyes AD, Aoki C. 2006. Nicotinic and muscarinic reduction of unitary excitatory postsynaptic potentials in sensory cortex; dual intracellular recording in vitro. *J Neurophysiol*. 95:2155–2166.

Lubke J, Feldmeyer D. 2007. Excitatory signal flow and connectivity in a cortical column: focus on barrel cortex. *Brain Struct Funct*. 212:3–17.

Ma S, Hangya B, Leonard CS, Wisden W, Gundlach AL. 2018. Dual-transmitter systems regulating arousal, attention, learning and memory. *Neurosci Biobehav Rev*. 85:21–33.

Mansvelder HD, McGehee DS. 2000. Long-term potentiation of excitatory inputs to brain reward areas by nicotine. *Neuron*. 27:349–357.

Marx M, Gunter RH, Hucko W, Radnikow G, Feldmeyer D. 2012. Improved biocytin labeling and neuronal 3D reconstruction. *Nat Protoc*. 7:394–407.

Mattinson CE, Burmeister JJ, Quintero JE, Pomerleau F, Huettl P, Gerhardt GA. 2011. Tonic and phasic release of glutamate and acetylcholine neurotransmission in sub-regions of the rat prefrontal cortex using enzyme-based microelectrode arrays. *J Neurosci Methods*. 202:199–208.

Mazzaferro S, Bermudez I, Sine SM. 2017. Alpha4beta2 nicotinic acetylcholine receptors: relationships between subunit stoichiometry and function at the single channel level. *J Biol Chem*. 292:2729–2740.

McCormick DA, Prince DA. 1985. Two types of muscarinic response to acetylcholine in mammalian cortical neurons. *Proc Natl Acad Sci U S A*. 82:6344–6348.

Mednikova YS, Karnup SV, Loseva EV. 1998. Cholinergic excitation of dendrites in neocortical neurons. *Neuroscience*. 87:783–796.

Mercer A, West DC, Morris OT, Kirchhecker S, Kerkhoff JE, Thomson AM. 2005. Excitatory connections made by presynaptic cortico-cortical pyramidal cells in layer 6 of the neocortex. *Cereb Cortex*. 15:1485–1496.

Mesulam MM, Mufson EJ, Wainer BH, Levey AI. 1983. Central cholinergic pathways in the rat: an overview based on an alternative nomenclature (Ch1-Ch6). *Neuroscience*. 10:1185–1201.

Narayanan RT, Egger R, Johnson AS, Mansvelder HD, Sakmann B, de Kock CP, Oberlaender M. 2015. Beyond columnar organization: cell type- and target layer-specific principles of horizontal axon projection patterns in rat vibrissal cortex. *Cereb Cortex*. 25:4450–4468.

Oberlaender M, de Kock CP, Bruno RM, Ramirez A, Meyer HS, Dercksen VJ, Helmstaedter M, Sakmann B. 2012. Cell type-specific three-dimensional structure of thalamocortical circuits in a column of rat vibrissal cortex. *Cereb Cortex*. 22:2375–2391.

Obermayer J, Verhoog MB, Luchicchi A, Mansvelder HD. 2017. Cholinergic modulation of cortical microcircuits is layer-specific: evidence from rodent, monkey and human brain. *Front Neural Circuits*. 11:100.

Oldford E, Castro-Alamancos MA. 2003. Input-specific effects of acetylcholine on sensory and intracortical evoked responses in the "barrel cortex" in vivo. *Neuroscience*. 117: 769–778.

Parikh V, Kozak R, Martinez V, Sarter M. 2007. Prefrontal acetylcholine release controls cue detection on multiple timescales. *Neuron*. 56:141–154.

Paul S, Jeon WK, Bizon JL, Han JS. 2015. Interaction of basal forebrain cholinergic neurons with the glucocorticoid system in stress regulation and cognitive impairment. *Front Aging Neurosci*. 7:43.

Pepeu G, Giovannini MG. 2004. Changes in acetylcholine extracellular levels during cognitive processes. *Learn Mem*. 11:21–27.

Pichon F, Nikonenko I, Kraftsik R, Welker E. 2012. Intracortical connectivity of layer VI pyramidal neurons in the somatosensory cortex of normal and barrelless mice. *Eur J Neurosci*. 35:855–869.

Poorthuis RB, Bloem B, Schak B, Wester J, de Kock CP, Mansvelder HD. 2013. Layer-specific modulation of the prefrontal cortex by nicotinic acetylcholine receptors. *Cereb Cortex*. 23: 148–161.

Qi G, Radnikow G, Feldmeyer D. 2015. Electrophysiological and morphological characterization of neuronal microcircuits in acute brain slices using paired patch-clamp recordings. *J Vis Exp*. 95:e52358. doi:10.3791/52358.

Radnikow G, Feldmeyer D. 2018. Layer- and cell type-specific modulation of excitatory neuronal activity in the Neocortex. *Front Neuroanat*. 12:1.

Ramaswamy S, Colangelo C, Markram H. 2018. Data-driven Modeling of cholinergic modulation of neural microcircuits: bridging neurons, synapses and network activity. *Front Neural Circuits*. 12:77.

Sarter M, Parikh V, Howe WM. 2009. Phasic acetylcholine release and the volume transmission hypothesis: time to move on. *Nat Rev Neurosci*. 10:383–390.

Sillito AM, Jones HE. 2002. Corticothalamic interactions in the transfer of visual information. *Philos Trans R Soc Lond Ser B Biol Sci*. 357:1739–1752.

Sundberg SC, Lindstrom SH, Sanchez GM, Granseth B. 2018. Cre-expressing neurons in visual cortex of Ntsr1-Cre GN220 mice are corticothalamic and are depolarized by acetylcholine. *J Comp Neurol*. 526:120–132.

Takacs VT, Freund TF, Nyiri G. 2013. Neuroligin 2 is expressed in synapses established by cholinergic cells in the mouse brain. *PLoS One*. 8:e72450.

Tasic B, Menon V, Nguyen TN, Kim TK, Jarsky T, Yao Z, Levi B, Gray LT, Sorensen SA, Dolbeare T *et al*. 2016. Adult mouse cortical cell taxonomy revealed by single cell transcriptomics. *Nat Neurosci*. 19:335–346.

Teles-Grilo Ruivo LM, Baker KL, Conway MW, Kinsley PJ, Gilmour G, Phillips KG, Isaac JTR, Lowry JP, Mellor JR. 2017. Coordinated acetylcholine release in prefrontal cortex and hippocampus is associated with arousal and reward on distinct timescales. *Cell Rep*. 18:905–917.

Thiele A. 2013. Muscarinic signaling in the brain. *Annu Rev Neurosci*. 36:271–294.

Thomson AM. 2010. Neocortical layer 6, a review. *Front Neuroanat*. 4:13.

Tian MK, Bailey CD, Lambe EK. 2014. Cholinergic excitation in mouse primary vs. associative cortex: region-specific magnitude and receptor balance. *Eur J Neurosci*. 40:2608–2618.

Urban-Ciecko J, Jouhanneau JS, Myal SE, Poulet JFA, Barth AL. 2018. Precisely timed nicotinic activation drives SST inhibition in neocortical circuits. *Neuron*. 97:611.

van Aerde KI, Qi GX, Feldmeyer D. 2015. Cell type-specific effects of adenosine on cortical neurons. *Cereb Cortex*. 25:772–787.

Wada E, Wada K, Boulter J, Deneris E, Heinemann S, Patrick J, Swanson LW. 1989. Distribution of alpha 2, alpha 3, alpha 4, and beta 2 neuronal nicotinic receptor subunit mRNAs in the central nervous system: a hybridization histochemical study in the rat. *J Comp Neurol*. 284:314–335.

West DC, Mercer A, Kirchhecker S, Morris OT, Thomson AM. 2006. Layer 6 cortico-thalamic pyramidal cells preferentially innervate interneurons and generate facilitating EPSPs. *Cereb Cortex*. 16:200–211.

Wester JC, Contreras D. 2013. Differential modulation of spontaneous and evoked thalamocortical network activity by acetylcholine level in vitro. *J Neurosci*. 33:17951–17966.

Yang Q, Chen CC, Ramos RL, Katz E, Keller A, Brumberg JC. 2014. Intrinsic properties of and thalamocortical inputs onto identified corticothalamic-VPM neurons. *Somatosens Mot Res*. 31:78–93.

Zaborszky L, Csordas A, Mosca K, Kim J, Gielow MR, Vadasz C, Nadasdy Z. 2015. Neurons in the basal forebrain project to the cortex in a complex topographic organization that reflects corticocortical connectivity patterns: an experimental study based on retrograde tracing and 3D reconstruction. *Cereb Cortex*. 25:118–137.

Zhang ZW, Deschenes M. 1997. Intracortical axonal projections of lamina VI cells of the primary somatosensory cortex in the rat: a single-cell labeling study. *J Neurosci*. 17:6365–6379.

Zhang Z, Seguela P. 2010. Metabotropic induction of persistent activity in layers II/III of anterior cingulate cortex. *Cereb Cortex*. 20:2948–2957.